Article
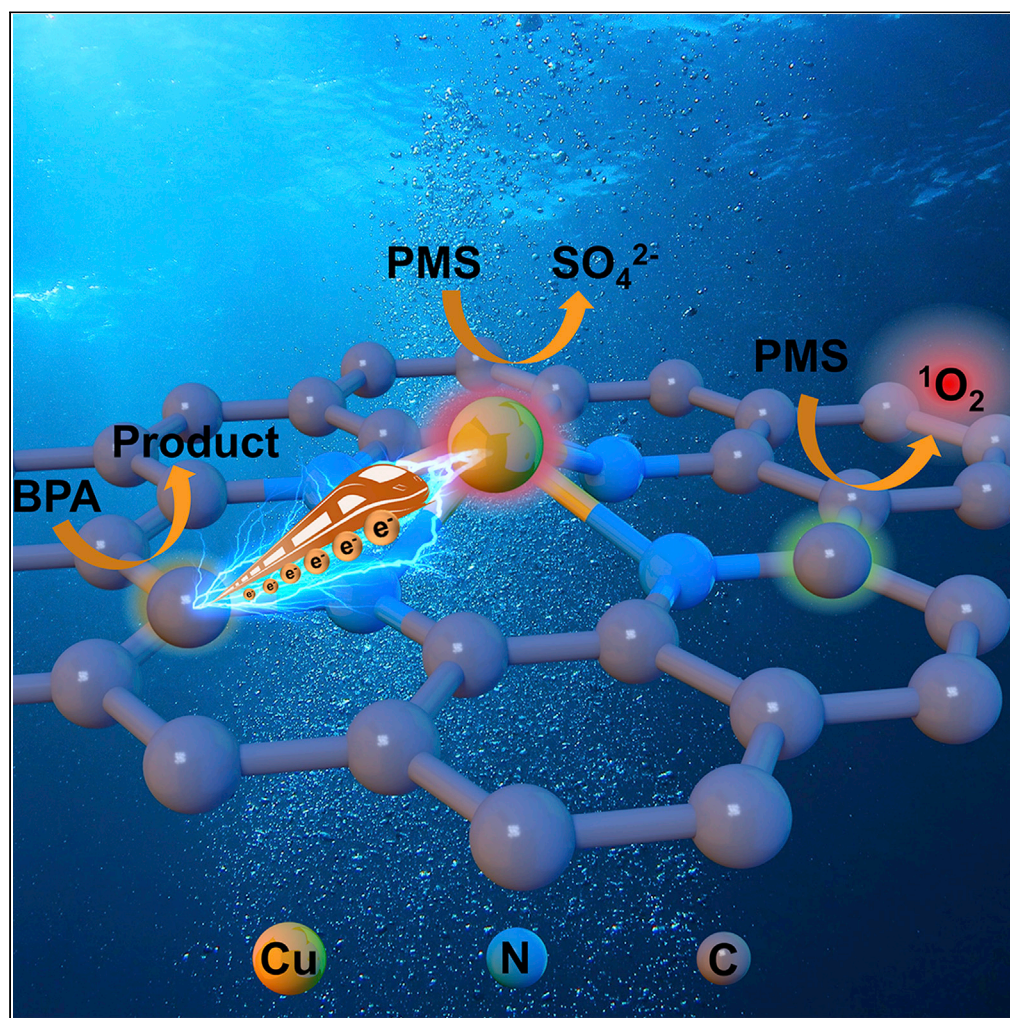
Insights into singlet oxygen generation and electron-transfer process induced by a single-atom Cu catalyst with saturated Cu-N$_4$ sites

Zhicong Lu, Peng Zhang, Chun Hu, Fan Li

lifan@gzhu.edu.cn

Highlights

Single-atom Cu catalyst with Cu-N$_4$ sites (SA-Cu-NC) was constructed

The saturated Cu-N$_4$ configuration provides two PMS activation sites

$^1O_2$ and electron transfer process were the dominant PMS activation pathways

Dual nonradical pathways exhibited superiority for pollutant degradation

Article

Insights into singlet oxygen generation and electron-transfer process induced by a single-atom Cu catalyst with saturated Cu-N$_4$ sites

Zhicong Lu,[1] Peng Zhang,[1] Chun Hu,[1] and Fan Li[1,2,*]

SUMMARY

Persulfate-based nonradical oxidation processes are appealing in water treatment for the efficient and selective degradation of trace contaminants in complex water matrices. However, there is still lacking of systematic understanding of the relationship between multiple nonradical pathways and the active sites of catalyst. Herein, a single-atom Cu catalyst with saturated Cu-N$_4$ sites on a carbon substrate (SA-Cu-NC) was constructed to activate peroxymonosulfate (PMS), which exhibited high catalytic performance and selectivity for pollutant degradation in different water conditions. Combined with the results of density functional theory (DFT) calculations, the electron-rich area around Cu site and the electron-poor area around C site in the saturated Cu-N$_4$ configuration could efficiently adsorb and activate PMS, which promoted pollutant degradation through the oxidation of singlet oxygen ($^1O_2$) and electron transfer process, respectively. This study advances the understanding of the saturated coordination structure of metals and the superiority of multiple nonradical pathways in wastewater treatment.

INTRODUCTION

In recent decades, emerging micropollutants in water have posed a serious threat to the ecological environment and human health, even at trace concentrations (ng L^{-1}–μg L^{-1}) (Schulze et al., 2019). Owing to the generation of powerful oxidizing radicals (e.g., hydroxyl radical $^•OH$ and sulfate radical $SO_4^{•-}$), persulfate-mediated advanced oxidation processes (AOPs) are regarded as efficient technologies for water purification (Wang et al., 2021a; Zhang et al., 2021). However, in actual water with complex chemical compositions, radicals are inevitably consumed by natural organic matter (NOM) and inorganic substrates (e.g., HCO_3^- and Cl^-), hindering the degradation of target pollutant and increasing the toxicity caused by halogenated byproducts (Yang et al., 2021). Therefore, selective degradation of emerging micropollutants in complex water matrices remains a significant challenge for water treatment.

Compared to radical-based advanced oxidation processes, nonradical processes exhibit high selectivity toward various substances in actual water. For instance, $^1O_2$ (E^0 = 2.2 V vs NHE) is identified as the dominant active oxidant for the degradation of bisphenol A in an oxygen vacancy-mediated BiOBr/PDS activation process (Bu et al., 2021; Qi et al., 2021). The electron transfer process has also been reported in the recent studies (Ren et al., 2020b, 2022). Both the pollutant and persulfate are effectively bonded on the catalyst surface to form a charge transfer complex, in which the catalyst plays a critical role in mediating electron transfer from the pollutant to persulfate. As oxidizing intermediate species, high-valent metal species (e.g., Fe(IV) and Co(IV)) can directly oxidize pollutants (Liu et al., 2021; Wang et al., 2022a). The coexistence of multiple nonradical pathways in a catalyst-persulfate system may further improve its application potential for complex wastewater treatment. Therefore, it is crucial to adopt effective approaches to identify active sites and persulfate activation pathways in the multiple nonradical pathways. Benefiting from the development of theoretical calculations, the adsorption sites and adsorption energy (E_{ads}) of persulfate on the catalyst are regarded as important indicators for determining the active sites of the catalyst and the activation processes of persulfate (Cui et al., 2021). The combination of experimental characterizations and theoretical calculations will be conducive to an in-depth exploration of the reaction mechanism. However, the coexistence of multiple species, especially the metal-based catalysts, limits the precise analysis of their structures and mechanisms.
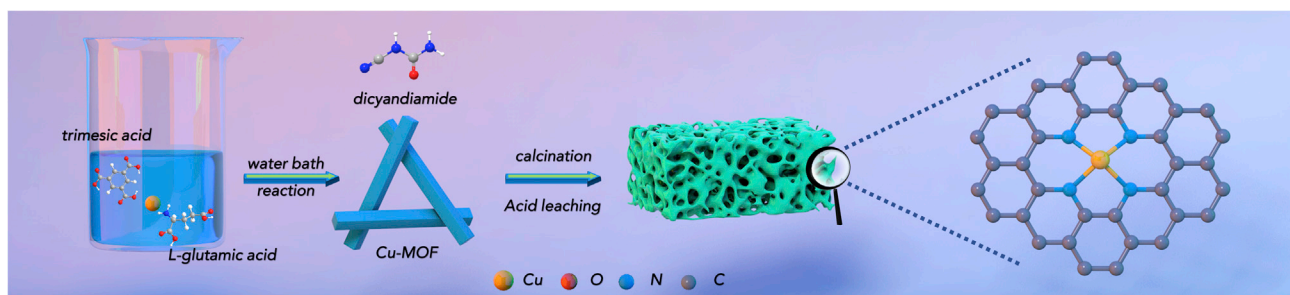
Figure 1. Schematic illustration of the synthesis process for SA-Cu-NC

Single-atom catalysts (SACs) have emerged as peroxymonosulfate (PMS) activators for pollutant degradation owing to their high atom utilization efficiency, dispersive active sites, and tunable electronic structures. For instance, Li et al. demonstrated that single-atom cobalt anchored on porous N-doped graphene reduced the migration distance of the active singlet oxygen produced from PMS activation, thus improving Fenton-like catalytic performance (Li et al., 2018). The electron transfer pathway was determined to be the dominant mechanism in the single-atom Cu catalyst SACu@NBC+PMS system, which differed from the traditional metal-based catalyst+PMS system (Pan et al., 2021). The uniform single-atom metal sites provide an ideal object for the identification of active sites and the study of reaction mechanisms through experimental characterizations and theoretical calculations (Li et al., 2022). A recent study showed that the saturated coordination of M-N-C single-atom catalysts did not significantly affect the PMS adsorption energy between the metal and non-metal sites (Wang et al., 2021b). The adsorption of PMS at multiple sites may induce diverse nonradical pathways of PMS activation, improving the activity and selectivity of pollutant degradation. However, relevant reports on the use of SACs for PMS activation via multiple nonradical pathways at different adsorption sites are still rare, and the corresponding mechanism deserves further analysis.

Herein, we developed a single-atom Cu catalyst (SA-Cu-NC) supported by N-doped carbon nanosheets by constructing saturated $Cu-N_4$ sites for the efficient catalytic oxidation of bisphenol A (BPA) with PMS activation. Based on the results of experimental characterizations and DFT calculations, PMS showed similar adsorption properties at the C and Cu sites. Unlike conventional radical mechanisms, $^1O_2$ oxidation and electron transfer process were the dominant PMS activation pathways on the two active sites in the SA-Cu-NC+PMS system. Based on the dual nonradical pathways, the SA-Cu-NC catalyst exhibited good catalytic properties and high selectivity for the degradation of emerging micropollutants under various anions, aquatic systems, and even actual wastewater conditions.

RESULTS AND DISCUSSION

Synthesis and structural characterizations of SA-Cu-NC

The SA-Cu-NC catalyst with isolated dispersed Cu atoms was prepared by the pyrolysis of a mixture of dicyandiamide (DCDA) and Cu-based metal-organic framework (Cu-MOF) (Figure 1). To effectively stabilize the Cu atoms for atomic dispersion, Cu-MOF with a typical stick-like shape (Figure S1) was synthesized via a liquid-phase reaction between Copper(II) acetate monohydrate ($Cu(CH_3COO)_2 \cdot H_2O$), L-glutamic acid, and trimesic acid. The SA-Cu-NC catalyst was finally obtained by calcining a mixture of Cu-MOF and DCDA under Ar condition, followed by acid etching to remove copper oxide.

As shown in the XRD patterns (Figure 2A), SA-Cu-NC and NC both exhibit two main broad peaks at 26.4° and 43.9°, assigned to the (002) and (004) planes of graphitic carbon, respectively (Zhu et al., 2020). In contrast to the XRD pattern of NC with Cu clusters (NP-Cu-NC) (Figure S2), no additional peaks corresponding to the Cu^0 particles and Cu_xO are observed. As illustrated in the HRTEM image (Figure 2B), SA-Cu-NC exhibits a 2D carbon nanosheet structure with obvious wrinkles. However, obvious Cu clusters appear in NP-Cu-NC (Figure S3), which is consistent with the result of XRD pattern (Figure S2). Additionally, the insignificant alteration in the Raman and FTIR spectra of NC and SA-Cu-NC indicates that the introduction of Cu exerts a negligible influence on the structure of the carbon framework (Figures S4 and S5) (Gao et al., 2021b). Figure 2C shows that numerous well-isolated atoms marked with red circles are observed in the aberration-corrected HAADF-STEM image, confirming that the Cu species in SA-Cu-NC exist as single atoms (Wu et al., 2022). Additionally, the EDX mapping images (Figures 2D–2G) of SA-Cu-NC further reveal
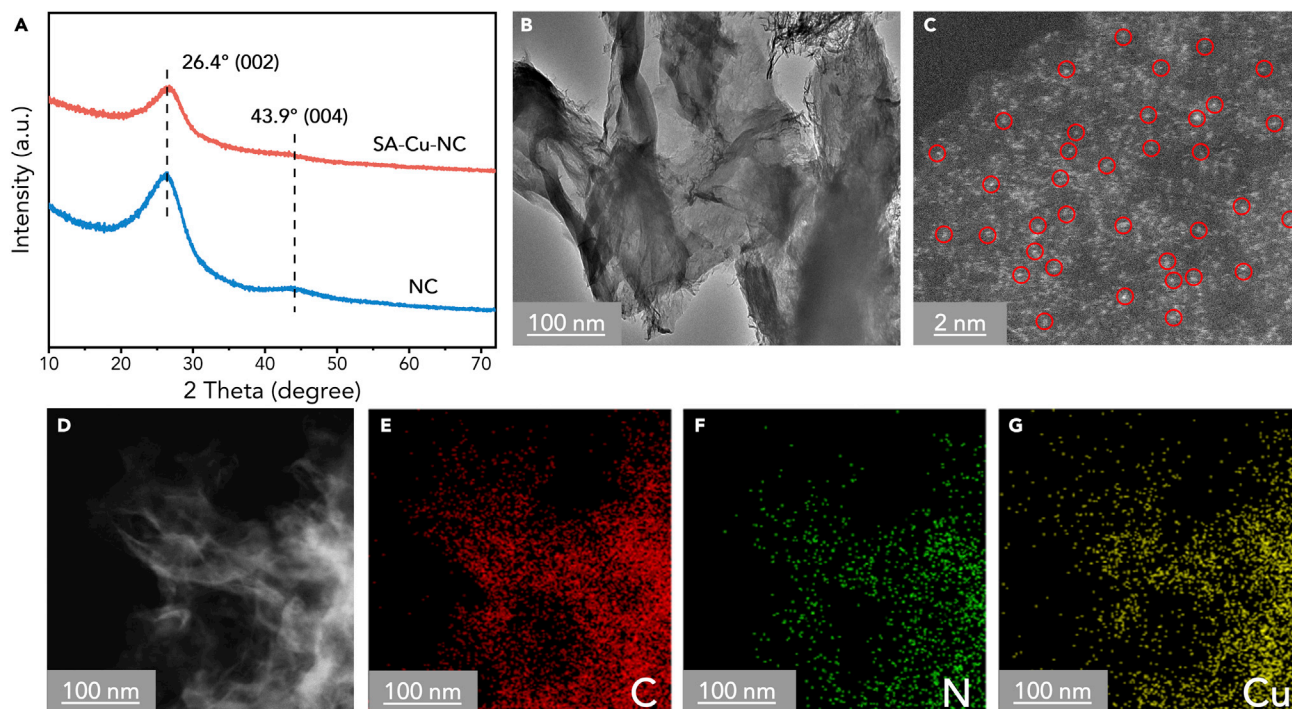
Figure 2. Structural characterizations of SA-Cu-NC

(A) X-ray diffraction (XRD) patterns of NC and SA-Cu-NC.

(B) High-resolution transmission electron microscopy (HRTEM) image of SA-Cu-NC.

(C) Aberration-corrected high-angle annular dark-field scanning transmission electron microscopy (HAADF-STEM) image of SA-Cu-NC.

(D–G) Energy-dispersive X-ray (EDX) images of SA-Cu-NC.

that Cu and N atoms are uniformly dispersed over the entire carbon substrate. These results demonstrate the successful synthesis of a single-atom Cu catalyst supported by an N-doped carbon substrate. As seen in the Cu $2p$ XPS spectrum of SA-Cu-NC (Figure 3A), the Cu $2p_{3/2}$ and Cu $2p_{1/2}$ peaks are deconvoluted into two peaks with binding energies of 954.5/952.2 eV and 934.7/932.4 eV, respectively, which are assigned to Cu(I) and Cu(II) (Guan et al., 2020). The shake-up satellite peak also confirms the presence of Cu(II). The total Cu content of SA-Cu-NC was determined to be 1.9 wt. % using ICP-OES. As shown in Figure S6, the four peaks in the N $1s$ spectrum of SA-Cu-NC represent pyridinic N (398.2 eV), pyrrolic N (399.4 eV), graphitic N (400.8 eV), and oxidized N species (404.0 eV), respectively. The peak located at 399.8 eV indicates the co-ordination of N and Cu atoms, suggesting the existence of Cu-N bonds in the SA-Cu-NC sample (Ren et al., 2020a). Cu K-edge XAFS spectra were obtained to determine the chemical state and coordination environment of Cu atoms in the SA-Cu-NC sample. Standard Cu foil, CuO, Cu_2O, and Cu(II) phthalocyanine (CuPc) samples were used as references. As seen in the XANES spectra (Figure 3B), the Cu-K absorption edge energy of SA-Cu-NC is located between those of Cu_2O and CuO, indicating that the Cu valence is between +1 and +2 (Pan et al., 2021). This is consistent with the XPS results (Figure 3A). In Figure 3C, the k^3-weight FT-EXAFS spectrum of SA-Cu-NC displays a main peak at ∼1.50 Å, which is corresponding to the Cu-N first shell (Zhu et al., 2020). The peaks at ∼2.20 Å and ∼1.53 Å assigned to the Cu-Cu and the Cu-O coordination, respectively, are not observed, suggesting that Cu atoms are separated from each other and coordinated with N atoms, consistent with the results of XRD, HAADF-STEM, and XPS (Figures 2A, 2C, and 3A). Furthermore, the quantitative EXAFS fitting results show that the average Cu-N coordination number of Cu in SA-Cu-NC is close to 4 and the average length of the Cu-N bond is approximately 1.96 Å (Figure 3D and Table S1). The WT-EXAFS images (Figures 3E and 3F) further corroborate the existence of the sole Cu-N bonds in SA-Cu-NC, which is distinguished from the Cu foil.

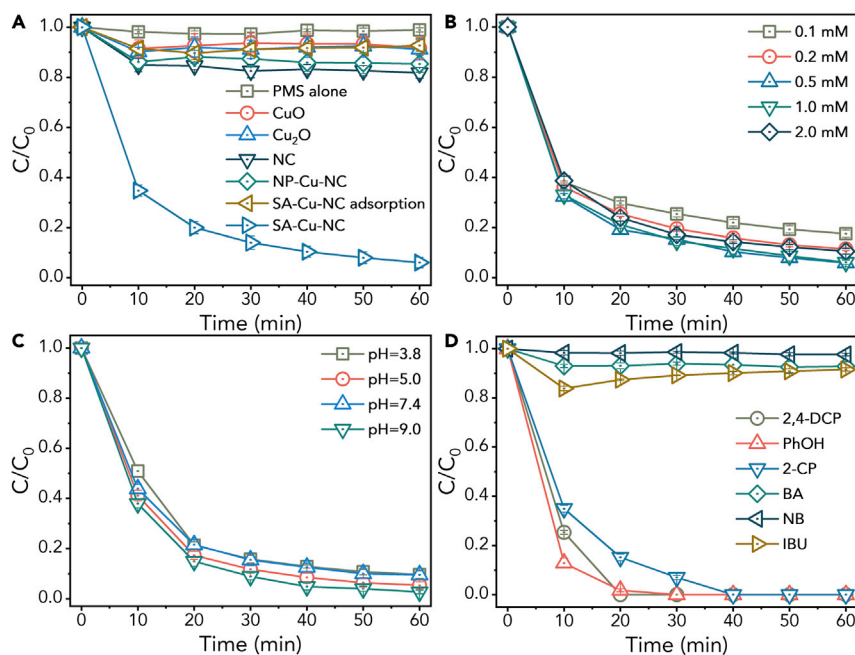### Catalytic performance of SA-Cu-NC for pollutant degradation

To evaluate the catalytic performance of SA-Cu-NC in PMS activation and pollutant degradation, BPA was selected as the target compound because of its frequent presence in the natural environment and potential
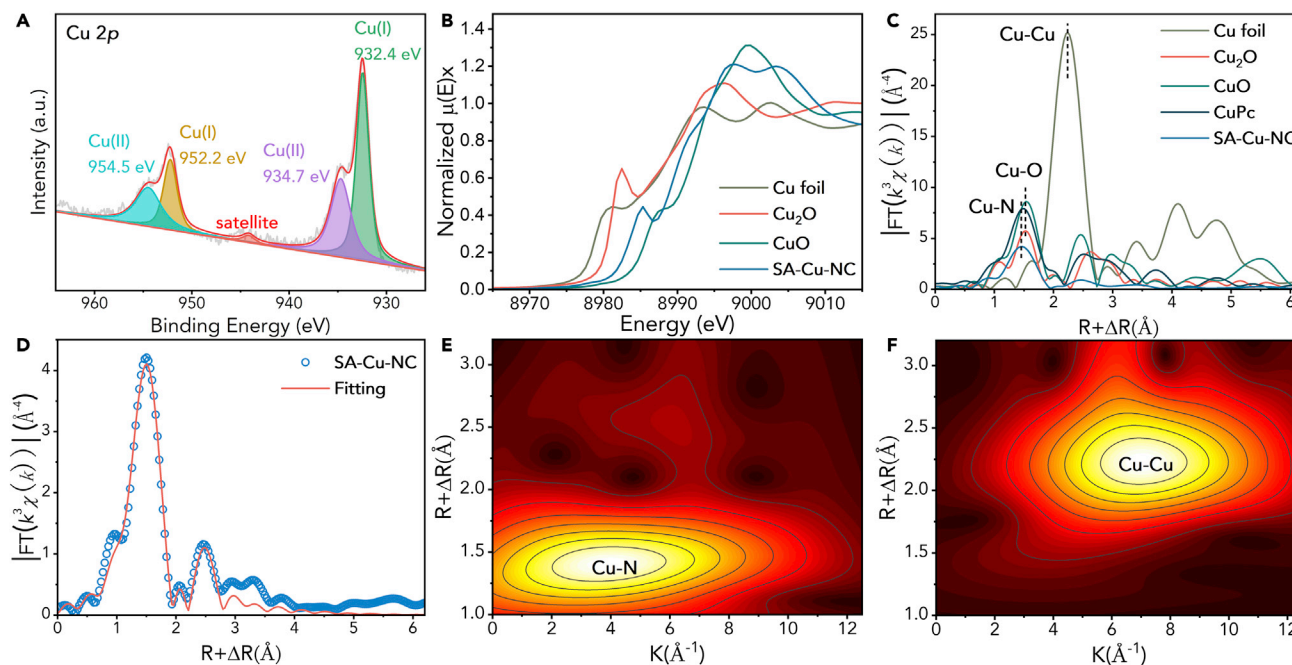
Figure 3. Chemical state and coordination structure of SA-Cu-NC

(A) X-ray photoelectron spectroscopy (XPS) Cu 2p spectrum of SA-Cu-NC.

(B) Normalized Cu K-edge X-ray absorption near-edge structure (XANES) spectra of SA-Cu-NC and reference samples.

(C) k^3-weight Fourier transform extended X-ray absorption fine structure (FT-EXAFS) spectra of SA-Cu-NC and reference samples.

(D) EXAFS R-space fitting curve of SA-Cu-NC.

(E) Wavelet transform (WT)-EXAFS spectrum of SA-Cu-NC.

(F) Wavelet transform (WT)-EXAFS spectrum of Cu foil.

harm to human beings (Santangeli et al., 2019). As shown in Figure 4A, more than 95% of BPA is removed within 60 min in the SA-Cu-NC+PMS system, whereas the degradation of BPA by PMS alone is negligible. The BPA can be completely removed by prolonging the reaction time or increasing the catalyst dosage (Figures S7A and S7B), indicating that the SA-Cu-NC+PMS system is efficient in degrading emerging contaminants with small concentrations for environmental purification. SA-Cu-NC achieves a quick adsorption-desorption equilibrium within 10 min, and only 10% of BPA is adsorbed on SA-Cu-NC surface. Notably, the NC sample can hardly activate PMS to degrade pollutants, indicating that the catalytic performance is remarkably improved by the introduction of single-atom Cu. In addition, less than 20% of BPA can be removed in the NP-Cu-NC, CuO, and Cu_2O systems within 60 min owing to the adsorption effect. In addition, the results of the same BPA concentration after storage for different periods demonstrate that 20 μL of sodium thiosulfate solution (0.1 mM) can completely quench the reaction (Figure S7C). In order to ensure the consistency of degradation test conditions of different batches, the reaction temperature was set at 30°C owing the negligible effects of the temperature variation of temperature from 20°C to 35°C (Figure S7D). A modified kinetic model (k value) considering the reaction rate constant, catalyst dosage, and pollutant concentration was used to compare the degradation rate of organic pollutants in various heterogeneous Fenton-like processes (Table S2). The k value of SA-Cu-NC+PMS (1.77 μmol $s^{-1}g^{-1}$) is remarkably higher than those of the other previously reported Cu-related heterogeneous Fenton-like catalysts (k value = 0.02–1.11 μmol $s^{-1}g^{-1}$) (Chen et al., 2020; Gao et al., 2021a; Jiang et al., 2018; Li et al., 2019; Song et al., 2021a, 2021b; Zhao et al., 2021). Consistent with the trend of BPA removal, the TOC removal efficiency reaches 80% in the SA-Cu-NC system within 60 min (Figure S7E), which is clearly better than those of the other reference systems (Cao et al., 2020; Pan et al., 2021). The transformation products (TPs) of BPA were identified using HPLC-MS (Figure S8), and two main oxidation pathways were proposed (Figure S9). Through a series of reactions, such as hydroxylation, deprotonation, and oxidative skeletal rearrangement, BPA can be converted to various ring-opened small molecules, which are eventually mineralized into CO_2 and H_2O. In addition, Figure 4B shows that the BPA removal rate is more than 80% with PMS concentration from 0.1 to 2.0 mM, which implies a high PMS utilization rate of SA-Cu-NC reducing the SO_4^{2-} emission.

Figure 4. Catalytic performance of SA-Cu-NC

(A) BPA degradation in various systems.

(B) Effect of PMS concentration on BPA degradation.

(C) Effect of pH values on BPA degradation.

(D) Degradation of different pollutants in the SA-Cu-NC+PMS system. Reaction conditions: [catalyst] = 0.04 g L^{-1}, [BPA]$_0$ = [2,4-DCP]$_0$ = [PhOH]$_0$ = [2-CP]$_0$ = [BA]$_0$ = [NB]$_0$ = [IBU]$_0$ = 50 μM (if any), [PMS]$_0$ = 1.0 mM, initial pH = 5.8 if not otherwise specified, Temp = 30°C.

To analyze the effect of pH values on the catalytic performance of SA-Cu-NC, a buffer solution was used to adjust the pH to avoid the rapid pH reduction caused by the addition of PMS. As shown in Figure 4C, SA-Cu-NC shows excellent BPA degradation performance, ranging from acidic to alkaline conditions. The negligible effect of pH values on BPA degradation indicates that the SA-Cu-NC+PMS system may have more than one reaction mechanism, which will be analyzed in the following part (i.e., **Identification of Active Oxidants**). Furthermore, the degradation kinetics of different pollutants (i.e., PhOH, 2,4-DCP, 2-CP, BA, NB, and IBU) in the SA-Cu-NC+PMS system was investigated (Figure 4D). The SA-Cu-NC+PMS system can effectively degrade PhOH, 2,4-DCP, and 2-CP, but shows ineffective degradation of BA, NB, and IBU, indicating that SA-Cu-NC prefers to attack electron-rich contaminants. The high selectivity for pollutant degradation implies the existence of nonradical pathways.

Identification of active oxidants

To determine the presence of reactive oxygen species in the SA-Cu-NC+PMS system, several scavenging tests were conducted. Methanol (MeOH) and *tert*-butanol (TBA) have been frequently employed as radical scavengers owing to their extremely high reactivity with free radicals (k (MeOH, $^{\bullet}$OH) = 9.7 × 10^8 M^{-1} s^{-1}, k (MeOH, SO$_4^{\bullet-}$) = 3.2 × 10^6 M^{-1} s^{-1}, and k (TBA, $^{\bullet}$OH) = 3.8–7.6 × 10^8 M^{-1} s^{-1}) (Huang and Zhang, 2019). As shown in Figure 5A, MeOH (1000 times the concentration of PMS) exhibits negligible impact on BPA degradation in the SA-Cu-NC+PMS system, indicating that $^{\bullet}$OH/SO$_4^{\bullet-}$ is not the main active species in the SA-Cu-NC system. However, TBA exhibits a slight inhibition of BPA degradation at 1000 times the PMS concentration, which may be due to the easy aggregation of the catalyst particles caused by the addition of TBA (Huang and Zhang, 2019). Furthermore, EPR analysis was performed to determine the presence of $^{\bullet}$OH and SO$_4^{\bullet-}$. As shown in Figure 5B, no characteristic signals of DMPO-$^{\bullet}$OH or DMPO-SO$_4^{\bullet-}$ can be observed in the SA-Cu-NC+PMS system, indicating the absence of $^{\bullet}$OH/SO$_4^{\bullet-}$ (Yun et al., 2018). However, a remarkable signal of DMPOX occurs in the SA-Cu-NC+PMS system, which is produced via the direct oxidation of DMPO involving nonradical processes rather than radical attack on DMPO (Wang et al., 2018). In addition, the intensity of the DMPOX signal significantly decreases with the addition of BPA, indicating that the oxidizing species can effectively degrade BPA.
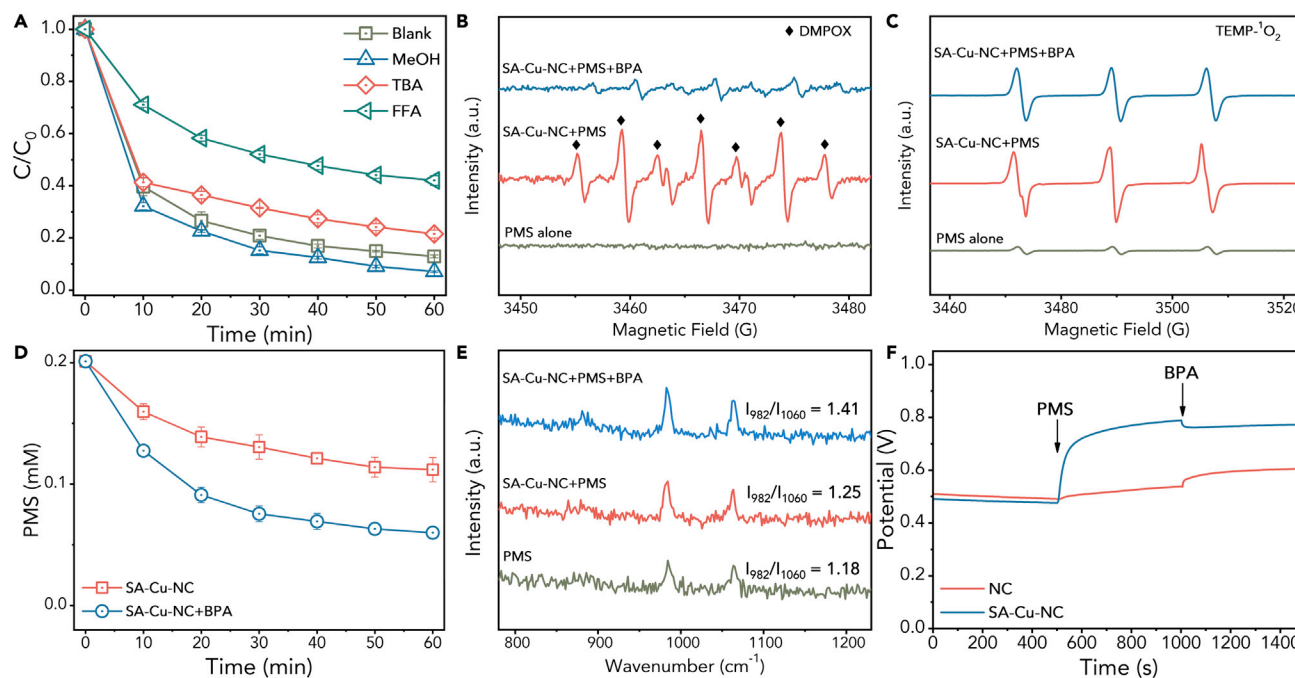
Figure 5. Identification of active oxidants

(A) Effect of MeOH, TBA, and FFA on BPA degradation in the SA-Cu-NC+PMS system.

(B) EPR spectra for ·OH/SO4·⁻ in the presence of DMPO in various systems.

(C) EPR spectra for $^1O_2$ in the presence of TEMP in various systems.

(D) Decomposition of PMS in various systems.

(E) *In situ* Raman spectra in various systems.

(F) The open-circuit potential (OCP) curves of NC and SA-Cu-NC. Reaction conditions: Reaction conditions: [catalyst] = 0.04 g L^{-1}, $[BPA]_0$ = 50 μM, $[PMS]_0$ = 1.0 mM, $[MeOH]_0$ = $[TBA]_0$ = 1000 mM, $[FFA]_0$ = 10 mM (if any), initial pH = 5.8, Temp = 30°C.

High-valent metal species (e.g., Fe(IV) and Co(IV)) have been identified as active oxidants for pollutant degradation, based on the oxygen atom transfer reaction, in which methyl phenyl sulfoxide (PMSO) can be readily oxidized to the corresponding sulfone product [methyl phenyl sulfone (PMSO₂)], which is significantly different from ·OH/SO4·⁻-mediated pathways (Qian et al., 2021; Wen et al., 2022). As shown in Figure S10, compared with PMS alone, the addition of SA-Cu-NC does not increase the generation of PMSO2, which suggests that Cu(III) may not be the active species in the SA-Cu-NC+PMS system. However, there are no related reports on the study of high-valent copper species Cu(III) based on the oxygen transfer reaction. To further determine the presence of Cu(III), *in situ* Raman spectroscopy was performed. The high-valent copper species Cu(III) can produce a characteristic band of Cu(III)-OH at approximately 610 cm^{-1} in the Raman spectrum (Jawad et al., 2020; Wang et al., 2020) (Figure S11). There is no obvious peak in the range of 200–600 cm^{-1}, further ruling out the generation of Cu(III).

$^1O_2$ is a mild and selective oxidizing species, which exhibits high reactivity toward electron-rich compounds (Qin et al., 2020). Therefore, the contribution of $^1O_2$ to pollutant degradation was investigated using FFA as the scavenger. As shown in Figure 5A, the removal efficiency of BPA decreases to 60% by adding 10 mM FFA (k (FFA, $^1O_2$) = 1.2 × 10^8 M^{-1} s^{-1}) to the SA-Cu-NC+PMS system, indicating the potential role of $^1O_2$. Furthermore, EPR spectra were used to detect the generation of $^1O_2$ in the SA-Cu-NC+PMS system. As shown in Figure 5C, the signal intensity of TEMP-$^1O_2$ considerably increases with the addition of PMS compared with that of the PMS alone and continues to increase over time (Figure S12), which suggests that PMS is activated by SA-Cu-NC for the generation of $^1O_2$. The obvious decrease in the signal caused by the addition of BPA further indicates that $^1O_2$ is the main active species for pollutant degradation. The involvement of $^1O_2$ was also investigated using D₂O instead of H₂O as the solvent, since the lifetime of $^1O_2$ in D₂O (20–32 μs) is more than 10-fold longer than that in H₂O (2 μs) (Zong et al., 2020). D₂O clearly enhances BPA degradation (Figure S13), and the markedly enhanced signal intensity of TEMP-$^1O_2$ is observed in D₂O (Figure S14), which further suggests that $^1O_2$ is responsible for BPA degradation.

In addition, N_2 and O_2 purging were used to drain dissolved oxygen and create oxygen-rich conditions in the BPA solution, respectively. Compared with the reaction in air, the oxygen-free and oxygen-rich conditions do not cause significant changes in BPA degradation (Figure S15), indicating that $^1O_2$ is completely converted from PMS rather than O_2. These results verify the key contribution of $^1O_2$ to the degradation of BPA in the SA-Cu-NC+PMS system.

For nonradical pathways, the electron transfer process is also a critical pathway for PMS activation and catalytic degradation. PMS directly abstracts electrons from the adsorbed organic pollutants on the catalyst surface, which results in the reduction of PMS to SO_4^{2-} rather than radicals ($^\cdot OH/SO_4^{\cdot -}$). The consumption of PMS with and without BPA was determined, as shown in Figure 5D. Without the addition of BPA, 0.08 mM PMS is consumed within 60 min, and this part of PMS should mainly be converted to $^1O_2$. Notably, the PMS consumption is further increased to approximately 0.15 mM with the addition of BPA, where the electrons of BPA are efficiently transferred to PMS through the electron bridge function of SA-Cu-NC. *In situ* Raman spectroscopy was used to analyze the PMS conversion process. As shown in Figure 5E, the peak at 1060 cm^{-1} is attributed to HSO_5^-, while the peak at 982 cm^{-1} is related to the symmetric stretching vibration mode of the S=O bond in SO_4^{2-}. The consumption of PMS can be evaluated by the variation in the ratio of the peak intensity at 982 cm^{-1} to that at 1060 cm^{-1} (I_{982}/I_{1060}), and a large ratio (I_{982}/I_{1060}) represents a large PMS consumption (Qian et al., 2021). After adding SA-Cu-NC into PMS solution, the ratio of I_{982}/I_{1060} increases from 1.18 to 1.25, implying the PMS consumption in the SA-Cu-NC system. In the presence of BPA, the ratio of I_{982}/I_{1060} further increases obviously from 1.25 to 1.41, indicating that the presence of BPA promotes the decomposition of PMS. Based on these results, it can be ascribed to a direct electron transfer process, in which SA-Cu-NC serves as the electron-transfer mediator between BPA and PMS, promoting the decomposition of PMS.

Electrochemical analysis can provide direct evidence of the electron transfer process. As shown in Figure 5F, the open-circuit potential (OCP) of SA-Cu-NC sharply rises with the addition of PMS and gradually reaches a plateau (potential of the SA-Cu-NC+PMS* complex). After the addition of BPA, electron transfer process of BPA to SA-Cu-NC+PMS* complex results in a decline of OCP, accompanied by the oxidation of BPA and reduction of PMS (Liang et al., 2021; Ren et al., 2022; Tan et al., 2020). In contrast, the potential of NC increases slightly upon the addition of PMS, and the subsequent addition of BPA causes an increase in the equilibrium potential. The results indicate that BPA does not donate electrons to NC and it just adsorb BPA to form a complex to further elevates the oxidation potential, which is consistent with the previous study (Wang et al., 2022b). Furthermore, as shown in the LSV curves (Figure S16), the current density increases continuously with the addition of PMS and BPA, further illustrating that electrons are transferred in the SA-Cu-NC+PMS+BPA system (Wang et al., 2019). The above results demonstrate the combined contributions of $^1O_2$ and the electron transfer process for BPA degradation in the SA-Cu-NC+PMS system.

The existence of dual nonradical pathways (i.e., $^1O_2$ and the electron transfer process) can explain that the SA-Cu-NC+PMS system is not affected by pH variation. pH can directly affect the charge on the catalyst surface, and then affect the adsorption of molecules and the subsequent degradation. As for the electron transfer process, high pH can increase the negative charge of catalyst, reducing the pollutant adsorption and inhibiting the pollutant degradation (Huang and Zhang, 2019). The isoelectric point of SA-Cu-NC is about 5.2 (Figure S17A). As shown in Figure S17B, the adsorption amount of BPA decreases in the SA-Cu-NC system with the increase of pH value and the adsorption trend of PMS should be similar, which cannot be directly measured owing to the PMS activation. The electron transfer process and corresponding BPA degradation should be suppressed in alkaline condition. Meanwhile, the acidic condition is favorable for the electron transfer process. The contribution of $^1O_2$ to pollutant degradation in various pH values was investigated using FFA as the scavenger. As shown in Figure S17C, with the increase of pH value from 3.8 to 9.0, the inhibition of FFA on BPA degradation is gradually enhanced, implying that the contribution of $^1O_2$ to pollutant degradation is gradually increased. Furthermore, EPR spectra were used to detect the generation of $^1O_2$ in various pH values. As shown in Figure S17D, the signal intensity of TEMP-$^1O_2$ in alkaline condition is significantly higher than that in acidic condition, which is consistent with the previous study (Bu et al., 2021). Although alkaline condition can inhibit the electron transfer process, it is beneficial to the generation of $^1O_2$. Similarly, although acidic condition is not conducive to the generation of $^1O_2$, the electron transfer process can be enhanced. Therefore, SA-Cu-NC shows excellent BPA degradation performance, ranging from acidic to alkaline conditions, which shows the superiority of the dual nonradical pathways compared with single nonradical process.

Mechanism in the SA-Cu-NC+PMS system

To elucidate the mechanism of PMS activation and BPA oxidization, the active sites of SA-Cu-NC and the corresponding PMS activation processes in the SA-Cu-NC+PMS system were explored. It has been reported that EDTA can poison isolated Cu sites in Cu-catalyzed reactions. As shown in Figure S18, with the addition of EDTA (0.5–5.0 mM), the BPA removal rate is obviously suppressed to 40% in the SA-Cu-NC+PMS system, indicating that single Cu atoms act as the active sites for the PMS conversion (Wang et al., 2020). The catalytic activity for BPA degradation does not further decrease, even though the concentration of EDTA is increased from 5.0 to 50.0 mM. This indicates that single-atom Cu is not the only active site, corresponding to the two proven PMS activation pathways. The generation of $^1O_2$ is derived from the oxidation of PMS, and the electron transfer process is dominated by the reduction of PMS.

In order to identify the active sites and PMS activation processes, DFT calculations were performed. As shown in Figure S19, the formation energy for the Cu-pyridinic N_4 model (0.06 eV) is much lower than that for the Cu-pyrrolic N_4 model (0.42 eV), demonstrating the more favorable construction of the Cu-pyridinic N_4 configuration. The mechanism of the dual nonradical pathways in the saturated Cu-N_4 coordination structure compared with the unsaturated Cu-N_2 coordination structure was further elucidated. As shown in Figure 6A_2 and 6B_2, the two-dimensional valence electron density images of Cu-N_4 and Cu-N_2 indicate that Cu and C atoms exhibit obvious valence electron polarization distribution. Cu site facilitates to donate electron to the adsorbent for reduction reaction, and C site tends to accept electron from the adsorbent for oxidation reaction. However, redox reactions occur only if PMS can be adsorbed at the two sites, which is also closely related to the specific coordination structure of the single-atom Cu. The PMS adsorption models on saturated Cu-N_4 and unsaturated Cu-N_2 coordination structures were analyzed. As shown in Figures 6A_3 and 6A_4, the minimal adsorption energy difference of 0.1 eV between Cu and C atoms on Cu-N_4 shows that PMS can be evenly distributed at Cu and C sites on Cu-N_4 configuration for the reduction reaction and oxidation reaction, corresponding to the electron transfer process and generation of $^1O_2$. In contrast, PMS mainly adsorbs on the Cu site of Cu-N_2 configurations owing to the obvious adsorption energy difference of 0.8 eV (Figures 6B_3 and 6B_4). The adsorption model is generally more favorable for PMS activation but restricts the adsorption and activation of PMS at other sites. Therefore, SA-Cu-NC with a saturated Cu-N_4 coordination structure provides two different PMS adsorption and activation sites. Specifically, when PMS adsorbs at the Cu site, electrons can be transferred from the electron-rich single-atom Cu site to PMS, enabling PMS reduction to directly produce SO_4^{2-}. Meanwhile, the BPA molecule adsorbed at the C site by π-π interactions donates electrons to SA-Cu-NC to realize its oxidative degradation. In addition, when PMS adsorbs on the C site, electrons transfer from PMS to the electron-poor C site, resulting in the generation of anion radical ($SO_5^{\bullet-}$), which rapidly converts to $^1O_2$ with water molecules involved in the oxidation of BPA. Therefore, both the electron transfer process and $^1O_2$ oxidation contribute to the efficient degradation of BPA.

Effect of complex matrices and durability based on continuous-flow test

Actual water contains various inorganic ions and natural organic matters (NOM), which inevitably affect the removal efficiency of target pollutants. To evaluate the feasibility of the SA-Cu-NC+PMS system, the effect of anions (Cl^-, HCO_3^-, $H_2PO_4^-$, SO_4^{2-}, and NO_3^-) and humid acid (HA) on the degradation of BPA was studied. As shown in Figure 6C, the inorganic anions (i.e., HCO_3^-, $H_2PO_4^-$, SO_4^{2-}, and NO_3^-) and HA have almost no influence on BPA degradation in the SA-Cu-NC+PMS system. The enhanced BPA degradation with Cl^- can be attributed to the generation of hypochlorite acid derived from the reaction of Cl^- and PMS, which was confirmed using the spectrophotometric N, N′-diethyl-p-phenylenediamine (DPD) method (Figure S20) (Gokulakrishnan et al., 2016; Wang and Wang, 2021). The removal of BPA in actual water (i.e., tap water and river water, water quality parameters are summarized in Table S3) was studied. Compared to the BPA removal efficiency in ultrapure water, the removal rate of BPA is not affected in tap and river water (Figure 6D), emphasizing the role of nonradical processes. This highlights the selectivity of the SA-Cu-NC+PMS system and confirms reduced interference of background inorganic and organic substances in the wastewater. Furthermore, the actual wastewater after the biological treatment (i.e., kitchen wastewater; water quality parameters are summarized in Table S3) was selected to evaluate the catalytic performance of SA-Cu-NC. In the 3D-EEM fluorescence spectra of kitchen wastewater (Figure S21), the original characteristic fluorescence peaks in areas A and B remarkably decrease, which demonstrates the effective destruction of aromatic protein-like substances in the SA-Cu-NC+PMS system for actual wastewater. The cycling test and corresponding characterizations were carried out to evaluate the stability of SA-Cu-NC. As shown in Figure S22A, 80% of BPA can still be removed within 60 min after five successive
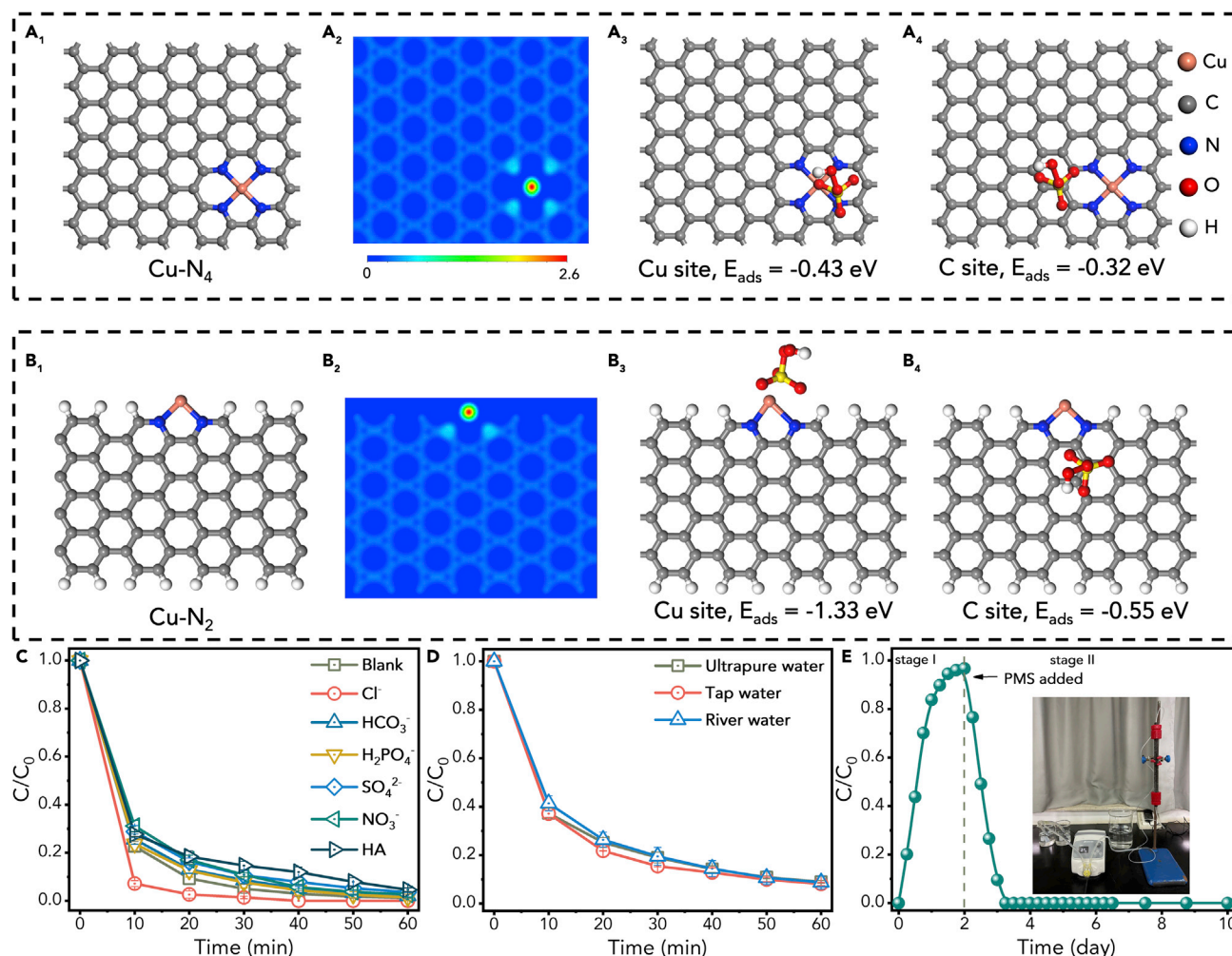
Figure 6. DFT calculations of PMS activation and durability of SA-Cu-NC

(A_1, B_1) The configuration models of $Cu-N_4$ and $Cu-N_2$.

(A_2, B_2) Two-dimensional valence-electron density images of $Cu-N_4$ and $Cu-N_2$.

(A_3, B_3) PMS adsorption model on Cu site of $Cu-N_4$ and $Cu-N_2$.

(A_4, B_4) PMS adsorption model on C site of $Cu-N_4$ and $Cu-N_2$.

(C) Effect of inorganic anions and humic acid on BPA degradation in the SA-Cu-NC+PMS system.

(D) Kinetics of BPA degradation with various actual water systems in the SA-Cu-NC+PMS system. Reaction conditions: [catalyst] = 0.04 g L^{-1}, $[BPA]_0$ = 50 μM, $[PMS]_0$ = 1.0 mM, $[anions]_0$ = 10 mM, $[HA]_0$ = 10 mg (if any), initial pH = 5.8, Temp = 30°C.

(E) BPA concentration in a continuous-flow reactor consisting of SA-Cu-NC filled column. Reaction conditions: [catalyst] = 50 mg, $[BPA]_0$ = 50 μM, $[PMS]_0$ = 1.0 mM, flow rate = 0.3 mL min^{-1}.

cycles, and the Cu concentration from Cu leaching is only 0.003 mg L^{-1}. XRD patterns show the used SA-Cu-NC maintains the basic structure (Figure S22B). The BET-specific surface area (SSA) of the used SA-Cu-NC decreases slightly owing to the collapse of some pore structure (Figures S22C and S22D). HRTEM spectrum and EDX mapping images indicate that the used SA-Cu-NC maintains the basic morphology and uniform distribution of Cu atoms (Figures S22E and S22F). Catalyst loss from sampling and recovery, release of Cu atoms, and reduction of SSA lead to the slight decrease of catalytic activity for BPA degradation. Furthermore, the durability of SA-Cu-NC was evaluated via a continuous-flow reaction using a column filled with SA-Cu-NC and silica sand. As illustrated in Figure 6E, without the addition of PMS, the column can basically reach saturation adsorption of BPA within 2 days. When PMS is added to the BPA solution, the BPA concentration in the effluent gradually decreases to undetectable levels within 1 day and remains constant for over 7 days. These results demonstrate that SA-Cu-NC exhibits good selectivity and durability for pollutant degradation.

Conclusions

In this study, a single-atom Cu catalyst with a saturated Cu-N$_4$ coordination structure was synthesized and utilized to activate PMS for pollutant degradation. The saturated Cu-N$_4$ configuration on the carbon substrate provided an electron-rich area around the Cu site and an electron-poor area around the C site. Benefiting from the saturated Cu-N$_4$ configuration, PMS can almost indistinguishably adsorb at these two sites and be activated through two different nonradical pathways, namely singlet oxygen and electron transfer process, which result in excellent catalytic activity and selectivity for pollutant degradation in complex matrices.

Limitations of the study

This study reports a single-atom Cu catalyst with saturated Cu-N$_4$ sites exhibiting high catalytic performance and selectivity for pollutant degradation under different anions, aquatic systems, and even actual wastewater conditions. However, the synthetic process is complicated and the cost of raw materials is high for the application of wastewater treatment. Therefore, further studies are needed to reduce the cost of raw materials and simplify the synthetic process to improve the application prospects for wastewater treatment.

STAR★METHODS

Detailed methods are provided in the online version of this paper and include the following:

- KEY RESOURCES TABLE
- RESOURCE AVAILABILITY
  - Lead contact
  - Materials availability
  - Data and code availability
- METHOD DETAILS
  - Material synthesis
  - Characterizations
  - Evaluation of the catalytic performance
  - The details of continuous-flow test
- QUANTIFICATION AND STATISTICAL ANALYSIS
  - The determination of Cu content in SA-Cu-NC
  - DFT calculations

SUPPLEMENTAL INFORMATION

Supplemental information can be found online at https://doi.org/10.1016/j.isci.2022.104930.

AUTHOR CONTRIBUTIONS

F.L. supervised the project and designed the experiments. Z.L. conducted all the experiments. P.Z. carried out the theoretical calculations. Z.L. and F.L. wrote and revised the manuscript. C.H. gave suggestions on the experiment and writing. All authors discussed and analyzed the data.

DECLARATION OF INTERESTS

The authors declare no competing financial interest.

CellPress
OPEN ACCESS

REFERENCES

Bu, Y., Li, H., Yu, W., Pan, Y., Li, L., Wang, Y., Pu, L., Ding, J., Gao, G., and Pan, B. (2021). Peroxydisulfate activation and singlet oxygen generation by oxygen vacancy for degradation of contaminants. Environ. Sci. Technol. 55, 2110–2120. https://doi.org/10.1021/acs.est.0c07274.

Cao, J., Yang, Z., Xiong, W., Zhou, Y., Wu, Y., Jia, M., Sun, S., Zhou, C., Zhang, Y., and Zhong, R. (2020). Peroxymonosulfate activation of magnetic Co nanoparticles relative to an N-doped porous carbon under confinement: boosting stability and performance. Separ. Purif. Technol. 250, 117237. https://doi.org/10.1016/j.seppur.2020.117237.

Chen, F., Wu, X.-L., Yang, L., Chen, C., Lin, H., and Chen, J. (2020). Efficient degradation and mineralization of antibiotics via heterogeneous activation of peroxymonosulfate by using graphene supported single-atom Cu catalyst. Chem. Eng. J. 394, 124904. https://doi.org/10.1016/j.cej.2020.124904.

Cui, P., Yang, Q., Liu, C., Wang, Y., Fang, G., Dionysiou, D.D., Wu, T., Zhou, Y., Ren, J., Hou, H., and Wang, Y. (2021). An N, S-anchored single-atom catalyst derived from domestic waste for environmental remediation. ACS EST. Eng. 1, 1460–1469. https://doi.org/10.1021/acsestengg.1c00255.

Delley, B. (1990). An all-electron numerical method for solving the local density functional for polyatomic molecules. J. Chem. Phys. 92, 508–517. https://doi.org/10.1063/1.458452.

Delley, B. (2000). From molecules to solids with the DMol3 approach. J. Chem. Phys. 113, 7756–7764. https://doi.org/10.1063/1.1316015.

Gao, P., Tian, X., Fu, W., Wang, Y., Nie, Y., Yang, C., and Deng, Y. (2021a). Copper in LaMnO3 to promote peroxymonosulfate activation by regulating the reactive oxygen species in sulfamethoxazole degradation. J. Hazard Mater. 411, 125163. https://doi.org/10.1016/j.jhazmat.2021.125163.

Gao, Y., Zhu, Y., Li, T., Chen, Z., Jiang, Q., Zhao, Z., Liang, X., and Hu, C. (2021b). Unraveling the high-activity origin of single-atom iron catalysts for organic pollutant oxidation via peroxymonosulfate activation. Environ. Sci. Technol. 55, 8318–8328. https://doi.org/10.1021/acs.est.1c01131.

Gokulakrishnan, S., Mohammed, A., and Prakash, H. (2016). Determination of persulphates using N, N-diethyl-p-phenylenediamine as colorimetric reagent: oxidative coloration and degradation of the reagent without bactericidal effect in water. Chem. Eng. J. 286, 223–231. https://doi.org/10.1016/j.cej.2015.10.058.

Guan, A., Chen, Z., Quan, Y., Peng, C., Wang, Z., Sham, T.-K., Yang, C., Ji, Y., Qian, L., Xu, X., and Zheng, G. (2020). Boosting CO2 electroreduction to CH4 via tuning neighboring single-copper sites. ACS Energy Lett. 5, 1044–1053. https://doi.org/10.1021/acsenergylett.0c00018.

Huang, K.Z., and Zhang, H. (2019). Direct electron-transfer-based peroxymonosulfate activation by iron-doped manganese oxide (delta-MnO2) and the development of galvanic oxidation processes (GOPs). Environ. Sci.

Technol. 53, 12610–12620. https://doi.org/10.1021/acs.est.9b03648.

Jawad, A., Zhan, K., Wang, H., Shahzad, A., Zeng, Z., Wang, J., Zhou, X., Ullah, H., Chen, Z., and Chen, Z. (2020). Tuning of persulfate activation from a free radical to a nonradical pathway through the incorporation of non-redox magnesium oxide. Environ. Sci. Technol. 54, 2476–2488. https://doi.org/10.1021/acs.est.9b04696.

Jiang, N., Lyu, L., Yu, G., Zhang, L., and Hu, C. (2018). A dual-reaction-center Fenton-like process on -C≡N-Cu linkage between copper oxides and defect-containing g-C3N4 for efficient removal of organic pollutants. J. Mater. Chem. 6, 17819–17828. https://doi.org/10.1039/C8TA04873H.

Koelling, D.D., and Harmon, B.N. (1977). A technique for relativistic spin-polarised calculations. J. Phys. C Solid State Phys. 10, 3107–3114. https://iopscience.iop.org/0022-3719/10/16/019.

Li, L., Hu, C., Zhang, L., Yu, G., Lyu, L., Li, F., and Jiang, N. (2019). Framework Cu-doped boron nitride nanobelts with enhanced internal electric field for effective Fenton-like removal of organic pollutants. J. Mater. Chem. 7, 6946–6956. https://doi.org/10.1039/C9TA00255C.

Li, X., Huang, X., Xi, S., Miao, S., Ding, J., Cai, W., Liu, S., Yang, X., Yang, H., Gao, J., et al. (2018). Single cobalt atoms anchored on porous N-Doped graphene with dual reaction sites for efficient Fenton-like catalysis. J. Am. Chem. Soc. 140, 12469–12475. https://doi.org/10.1021/jacs.8b05992.

Li, F., Lu, Z., Li, T., Zhang, P., and Hu, C. (2022). Origin of the excellent activity and selectivity of a single-atom copper catalyst with unsaturated Cu-N2 sites via peroxydisulfate activation: Cu(III) as a dominant oxidizing species. Environ. Sci. Technol. 56, 8765–8775. https://doi.org/10.1021/acs.est.2c00369.

Liang, J., Duan, X., Xu, X., Chen, K., Zhang, Y., Zhao, L., Qiu, H., Wang, S., and Cao, X. (2021). Persulfate oxidation of sulfamethoxazole by magnetic iron-char composites via nonradical pathways: Fe(IV) versus surface-mediated electron transfer. Environ. Sci. Technol. 55, 10077–10086. https://doi.org/10.1021/acs.est.1c01618.

Liu, B., Guo, W., Jia, W., Wang, H., Si, Q., Zhao, Q., Luo, H., Jiang, J., and Ren, N. (2021). PMSO novel nonradical oxidation of sulfonamide antibiotics with Co(II)-doped g-C3N4-activated peracetic acid: role of high-valent cobalt-oxo species. Environ. Sci. Technol. 55, 12640–12651. https://doi.org/10.1021/acs.est.1c04091.

Pan, J., Gao, B., Duan, P., Guo, K., Akram, M., Xu, X., Yue, Q., and Gao, Y. (2021). Improving peroxymonosulfate activation by copper ion-saturated adsorbent-based single atom catalysts for the degradation of organic contaminants: electron-transfer mechanism and the key role of Cu single atoms. J. Mater. Chem. 9, 11604–11613. https://doi.org/10.1039/D1TA02237G.

Perdew, J.P., Burke, K., and Ernzerhof, M. (1996). Generalized gradient approximation made

simple. Phys. Rev. Lett. 77, 3865–3868. https://doi.org/10.1103/PhysRevLett.77.3865.

Qi, Y., Li, J., Zhang, Y., Cao, Q., Si, Y., Wu, Z., Akram, M., and Xu, X. (2021). Novel lignin-based single atom catalysts as peroxymonosulfate activator for pollutants degradation: role of single cobalt and electron transfer pathway. Appl. Catal. B Environ. 286, 119910. https://doi.org/10.1016/j.apcatb.2021.119910.

Qian, K., Chen, H., Li, W., Ao, Z., Wu, Y.N., and Guan, X. (2021). Single-atom Fe Catalyst outperforms its homogeneous counterpart for activating peroxymonosulfate to achieve effective degradation of organic contaminants. Environ. Sci. Technol. 55, 7034–7043. https://doi.org/10.1021/acs.est.0c08805.

Qin, J., Dai, L., Shi, P., Fan, J., Min, Y., and Xu, Q. (2020). Rational design of efficient metal-free catalysts for peroxymonosulfate activation: selective degradation of organic contaminants via a dual nonradical reaction pathway. J. Hazard Mater. 398, 122808. https://doi.org/10.1016/j.jhazmat.2020.122808.

Ren, W., Cheng, C., Shao, P., Luo, X., Zhang, H., Wang, S., and Duan, X. (2022). Origins of electron-transfer regime in persulfate-based nonradical oxidation processes. Environ. Sci. Technol. 56, 78–97. https://doi.org/10.1021/acs.est.1c05374.

Ren, P., Li, Q., Song, T., and Yang, Y. (2020a). Facile fabrication of the Cu-N-C catalyst with atomically dispersed unsaturated Cu-N2 active sites for highly efficient and selective Glaser-Hay coupling. ACS Appl. Mater. Interfaces 12, 27210–27218. https://doi.org/10.1021/acsami.0c05100.

Ren, W., Xiong, L., Nie, G., Zhang, H., Duan, X., and Wang, S. (2020b). Insights into the electron-transfer regime of peroxydisulfate activation on carbon nanotubes: the role of oxygen functional groups. Environ. Sci. Technol. 54, 1267–1275. https://doi.org/10.1021/acs.est.9b06208.

Santangeli, S., Consales, C., Pacchierotti, F., Habibi, H.R., and Carnevali, O. (2019). Transgenerational effects of BPA on female reproduction. Sci. Total Environ. 685, 1294–1305. https://doi.org/10.1016/j.scitotenv.2019.06.029.

Schulze, S., Zahn, D., Montes, R., Rodil, R., Quintana, J.B., Knepper, T.P., Reemtsma, T., and Berger, U. (2019). Occurrence of emerging persistent and mobile organic contaminants in European water samples. Water Res. 153, 80–90. https://doi.org/10.1016/j.watres.2019.01.008.

Song, H., Guan, Z., Xia, D., Xu, H., Yang, F., Li, D., and Li, X. (2021a). Copper-oxygen synergistic electronic reconstruction on g-C3N4 for efficient non-radical catalysis for peroxydisulfate and peroxymonosulfate. Separ. Purif. Technol. 257, 117957. https://doi.org/10.1016/j.seppur.2020.117957.

Song, H., Liu, Z., Guan, Z., Yang, F., Xia, D., and Li, D. (2021b). Efficient persulfate non-radical activation of electron-rich copper active sites induced by oxygen on graphitic carbon nitride. Sci. Total Environ. 762, 143127. https://doi.org/10.1016/j.scitotenv.2020.143127.

Tan, W., Ren, W., Wang, C., Fan, Y., Deng, B., Lin, H., and Zhang, H. (2020). Peroxymonosulfate activated with waste battery-based Mn-Fe oxides for pollutant removal: electron transfer mechanism, selective oxidation and LFER analysis. Chem. Eng. J. *394*, 124864. https://doi.org/10.1016/j.cej.2020.124864.

Tkatchenko, A., and Scheffler, M. (2009). Accurate molecular van der Waals interactions from ground-state electron density and free-atom reference data. Phys. Rev. Lett. *102*, 073005. https://doi.org/10.1103/PhysRevLett.102.073005.

Wang, H., Guo, W., Liu, B., Wu, Q., Luo, H., Zhao, Q., Si, Q., Sseguya, F., and Ren, N. (2019). Edge-nitrogenated biochar for efficient peroxydisulfate activation: an electron transfer mechanism. Water Res. *160*, 405–414. https://doi.org/10.1016/j.watres.2019.05.059.

Wang, L., Jiang, J., Pang, S.-Y., Zhou, Y., Li, J., Sun, S., Gao, Y., and Jiang, C. (2018). Oxidation of bisphenol A by nonradical activation of peroxymonosulfate in the presence of amorphous manganese dioxide. Chem. Eng. J. *352*, 1004–1013. https://doi.org/10.1016/j.cej.2018.07.103.

Wang, Y., Lyu, L., Wang, D., Yu, H.Q., Li, T., Gao, Y., Li, F., Crittenden, J.C., Zhang, L., and Hu, C. (2021a). Cation-π induced surface cleavage of organic pollutants with $\cdot$OH formation from H_2O for water treatment. iScience *24*, 102874. https://doi.org/10.1016/j.isci.2021.102874.

Wang, Z., Qiu, W., Pang, S.Y., Guo, Q., Guan, C., and Jiang, J. (2022a). Aqueous iron(IV)-oxo complex: an emerging powerful reactive oxidant formed by iron(II)-based advanced oxidation processes for oxidative water treatment. Environ. Sci. Technol. *56*, 1492–1509. https://doi.org/10.1021/acs.est.1c04530.

Wang, J., and Wang, S. (2021). Effect of inorganic anions on the performance of advanced oxidation processes for degradation of organic contaminants. Chem. Eng. J. *411*, 128392. https://doi.org/10.1016/j.cej.2020.128392.

Wang, L., Wang, L., Shi, Y., Zhu, J., Zhao, B., Zhang, Z., Ding, G., and Zhang, H. (2022b). Fabrication of Co_3O_4-Bi_2O_3-Ti catalytic membrane for efficient degradation of organic pollutants in water by peroxymonosulfate activation. J. Colloid Interface Sci. *607*, 451–461. https://doi.org/10.1016/j.jcis.2021.08.086.

Wang, L., Xu, H., Jiang, N., Wang, Z., Jiang, J., and Zhang, T. (2020). Trace cupric species triggered decomposition of peroxymonosulfate and degradation of organic pollutants: Cu(III) being the primary and selective intermediate oxidant. Environ. Sci. Technol. *54*, 4686–4694. https://doi.org/10.1021/acs.est.0c00284.

Wang, S., Xu, L., and Wang, J. (2021b). Iron-based dual active site-mediated peroxymonosulfate activation for the degradation of emerging organic pollutants. Environ. Sci. Technol. *55*, 15412–15422. https://doi.org/10.1021/acs.est.1c06205.

Wen, Y., Huang, C.H., Ashley, D.C., Meyerstein, D., Dionysiou, D.D., Sharma, V.K., and Ma, X. (2022). Visible light-induced catalyst-free activation of peroxydisulfate: pollutant-dependent production of reactive species. Environ. Sci. Technol. *56*, 2626–2636. https://doi.org/10.1021/acs.est.1c06696.

Wu, X., Rigby, K., Huang, D., Hedtke, T., Wang, X., Chung, M.W., Weon, S., Stavitski, E., and Kim, J.H. (2022). Single-atom cobalt incorporated in a 2D graphene oxide membrane for catalytic pollutant degradation. Environ. Sci. Technol. *56*, 1341–1351. https://doi.org/10.1021/acs.est.1c06371.

Yang, Z., Qian, J., Shan, C., Li, H., Yin, Y., and Pan, B. (2021). Toward selective oxidation of contaminants in aqueous systems. Environ. Sci. Technol. *55*, 14494–14514. https://doi.org/10.1021/acs.est.1c05862.

Yun, E.T., Lee, J.H., Kim, J., Park, H.D., and Lee, J. (2018). Identifying the nonradical mechanism in the peroxymonosulfate activation process: singlet oxygenation versus mediated electron transfer. Environ. Sci. Technol. *52*, 7032–7042. https://doi.org/10.1021/acs.est.8b00959.

Zhang, Y., Yang, W., Zhang, K., Kumaravel, A., and Zhang, Y. (2021). Sulfite activation by glucose-derived carbon catalysts for As(III) oxidation: the role of ketonic functional groups and conductivity. Environ. Sci. Technol. *55*, 11961–11969. https://doi.org/10.1021/acs.est.1c02499.

Zhao, Y., Wang, H., Li, X., Yuan, X., Jiang, L., and Chen, X. (2021). Recovery of CuO/C catalyst from spent anode material in battery to activate peroxymonosulfate for refractory organic contaminants degradation. J. Hazard Mater. *420*, 126552. https://doi.org/10.1016/j.jhazmat.2021.126552.

Zhu, T., Chen, Q., Liao, P., Duan, W., Liang, S., Yan, Z., and Feng, C. (2020). Single-atom Cu catalysts for enhanced electrocatalytic nitrate reduction with significant alleviation of nitrite production. Small *16*, e2004526. https://doi.org/10.1002/smll.202004526.

Zong, Y., Guan, X., Xu, J., Feng, Y., Mao, Y., Xu, L., Chu, H., and Wu, D. (2020). Unraveling the overlooked involvement of high-valent cobalt-oxo Species generated from the cobalt(II)-activated peroxymonosulfate process. Environ. Sci. Technol. *54*, 16231–16239. https://doi.org/10.1021/acs.est.0c06808.

STAR★METHODS

KEY RESOURCES TABLE

REAGENT or RESOURCE	SOURCE	IDENTIFIER
Chemicals, peptides, and recombinant proteins		
Copper (II) acetate monohydrate	Adamas	CAS: 6046-93-1
1, 3, 5-benzenetricarboxylic acid	Adamas	CAS: 554-95-0
L-glutamic acid	Adamas	CAS: 56-86-0
Dicyandiamide	Adamas	CAS: 461-58-5
Copper (II) oxide	Shanghai Macklin	CAS: 1317-38-0
Copper (I) oxide	Shanghai Macklin	CAS: 1317-39-1
Peroxymonosulfate	Adamas	CAS: 70693-62-8
Sodium thiosulfate	Adamas	CAS: 7772-98-7
5,5-dimethyl-1-pyrroline-N-oxide	Dojindo	CAS: 3317-61-10
2,2,6,6-tetramethyl-4-piperidinol	Adamas	CAS: 2403-88-5
bisphenol A	Adamas	CAS: 80-05-7
2-chlorophenol	Adamas	CAS: 95-57-8
2,4-dichlorophenol	Adamas	CAS: 120-83-2
Phenol	Adamas	CAS: 108-95-2
Benzoic acid	Adamas	CAS: 65-85-0
Nitrobenzene	Adamas	CAS: 98-95-3
Ibuprofen	Adamas	CAS: 15687-27-1
Furfuryl alcohol	Adamas	CAS: 98-00-0
tert-Butanol	Adamas	CAS: 75-65-0
Methanol	Adamas	CAS: 67-56-1
Boric acid	Adamas	CAS: 10043-35-3
Odium tetraborate decahydrate	Adamas	CAS: 1303-96-4
Acetic acid	Shanghai Aladdin	CAS: 64-19-7
Sodium acetate	Adamas	CAS: 127-09-3
Humic acid	Shanghai Aladdin	CAS: 1415-93-6
Ethylenedinitrilotetraacetic acid	Adamas	CAS: 60-00-4
Software and algorithms		
Origin 2018	OriginLab	https://www.originlab.com/
Excel	Microsoft	N/A

RESOURCE AVAILABILITY

Lead contact

Further information and requests for resources and reagents should be directed to and will be fulfilled by the lead contact, Fan Li (lifan@gzhu.edu.cn).

Materials availability

This study did not generate new unique reagents.

Data and code availability

- Data reported in this paper will be shared by the lead contact upon request.

- This paper does not report original code.

- Any additional information required to reanalyze the data reported in this paper is available from the lead contact upon request.

METHOD DETAILS

Material synthesis

A single-atom Cu catalyst (SA-Cu-NC) was synthesized using a modified pyrolysis process (Zhu et al., 2020). First, benzenetricarboxylic acid (BTC, 5 mmol) was dissolved in ultrapure water (450 mL) and ethanol (50 mL) to form solution A. Under vigorous stirring, solution A was slowly added to 500 mL of solution B containing $Cu(CH_3COO)_2 \cdot H_2O$ (10 mmol) and L-glutamic acid (5 mmol) and stirred for 2 h. The obtained product was washed with ultrapure water and ethanol and then dried in vacuum at 60°C overnight. Afterward, the dried sample (0.10 g) and dicyandiamide (DCDA, 1.0 g) were mixed and ball-milled for 0.5 h followed by calcination at 800°C for 3 h under an Ar atmosphere at a heating rate of 3°C min^{-1}. Finally, the residual product was leached with 1.0 M H_2SO_4 for 12 h to obtain SA-Cu-NC. For comparison, BTC (0.10 g) and DCDA (1.0 g) were mixed via ball milling and calcined at 800°C using the same follow-up process, and the obtained sample was labeled as NC. For the synthesis of the catalyst with Cu clusters (NP-Cu-NC), Cu-MOF (1.00 g) was mixed with DCDA (1.00 g) via ball milling, following the same method as that for SA-Cu-NC.

Characterizations

The XRD patterns of all the samples were recorded in the range of 10°–80° (2θ) on a PANalytical X-ray diffractometer (PW3040/60) with Cu Kα radiation. High-resolution transmission electron microscopy (HRTEM) images and energy-dispersive X-ray spectroscopy (EDX) were applied to characterize the crystal morphology of the catalyst. Aberration-corrected high-angle annular dark-field scanning transmission electron microscopy (HAADF-STEM) images were recorded using a JEOL ARM200CF. The Raman spectra were collected on a LabRAM HR Evolution (HORIBA, France) equipped with a CCD detector utilizing a laser source at an excitation line of 532 nm. X-ray photoelectron spectroscopy (XPS) measurements were obtained using an ESCALAB 250Xi X-ray photoelectron spectroscope. The binding energies were calibrated with the C 1s hydrocarbon peak at 284.8 eV. The Cu K edge XAFS data were recorded under ambient temperature and pressure at the Singapore Synchrotron Light Source (SSLS) center, where a pair of channel-cut Si (111) crystals was used in the monochromator. The software Athena and Artemis were used to process and analyze the data. The concentration of copper in the catalyst was measured by inductively coupled plasma optical emission spectrometry (ICP-OES) (Avio 200, PerkinElmer). The EPR spectra were recorded on a Bruker A300-10/12 electron paramagnetic resonance spectrometer. The Brunauer-Emmett-Teller (BET) surface area was determined by performing N2 adsorption-desorption experiments using a physisorption analyzer (ASAP 2460, Micromeritics). Measurement of SO_4^{2-} was conducted by Thermo ICS-600 ion chromatography. Electrochemical measurements were performed in a standard three-electrode cell system on a CHI 700E electrochemical workstation. The ITO conductive glass coated with catalyst, Pt wire, and Ag/AgCl electrode were employed as working electrode, counter electrode, and reference electrode, respectively. The intermediate products of BPA degradation were detected using HPLC-MS (Agilent 1260-6460, USA).

Evaluation of the catalytic performance

The catalytic performance for pollutant degradation was tested in a 50-mL beaker under magnetic stirring at 30°C. Typically, the Cu single-atom catalyst (2.0 mg) and PMS (1.0 mM) were added to 50 mL of BPA solution (50 μM) and stirred. At specific intervals, 1.0 mL of suspension was withdrawn and filtered to the HPLC bottle through a 0.45 μm glass fiber filter, and 20 μL of sodium thiosulfate solution (0.1 mM) was added to quench the oxidizing species. The concentration of the organic pollutant was analyzed using a 1200 series HPLC system (Agilent, USA). The total organic carbon (TOC) of the solution was determined using a TOC-L CPH CN200 TOC analyzer (Shimadzu, Japan). To keep pH constant during the reaction in the pH experiments, the mixture of acetic acid and sodium acetate solution and that of boric acid and sodium borate solution were employed as the buffer for the reaction conducted at pHs 3.8 and 5.0–9.0, respectively (Huang and Zhang, 2019; Pan et al., 2021; Qian et al., 2021). In the cycling test, the catalyst was recycled after each run of the test by washing and filtration. Then the residual catalyst was added into the new BPA solution for PMS activation and BPA degradation.

The details of continuous-flow test

A silica tube (1.0 × 20.0 cm) was filled with 50 mg of SA-Cu-NC and a certain amount of silica sand to lower down the pressure for water passing through the column. The inlet and outlet were filed with 2.0 cm-thick silica sand to prevent the catalyst loss and the actual thickness of the column filled with the mixture of SA-Cu-NC and silica sand was about 16.0 cm. Then, the reaction solution was pumped through the column

using a peristaltic at a flow rate of 0.3 mL min^{-1} (0.8 r min^{-1}). The actual empty bed contact time (EBCT) was approximately 42 min.

QUANTIFICATION AND STATISTICAL ANALYSIS

The determination of Cu content in SA-Cu-NC

The determination process of Cu content in the SA-Cu-NC catalyst is as follows: 2 mg of the SA-Cu-NC catalyst was placed in a teflon crucible, then 2.0 mL of sulfuric acid and 3.0 mL nitric acid were added. The suspension was heated on a 150°C electric heating plate until the suspension became clear and transparent. After cooling to room temperature, the solution was transferred to a 50.0 mL volumetric flask, diluted with water to the volume, and shaken up well. Finally, 5.0 mL of solution was withdrawn and the Cu concentration was measured by an inductively coupled plasma emission spectrometry (ICP-OES). The Cu content in the SA-Cu-NC catalyst was calculated from Equation S1.

$$\text{Ratio}_{Cu} = \frac{c \times 0.05\ L}{2\ mg} \times 100\% \qquad \text{(Equation S1)}$$

Where c and Ratio$_{Cu}$ are the Cu concentration (mg L^{-1}) measured by ICP-OES and Cu content in the Cu-NC catalyst.

DFT calculations

All density functional theory calculations were performed by DMol^3 code (Delley, 1990, 2000). The exchange and correlation effect were described by the generalized gradient approximation (GGA) with the Perdew-Burke-Ernzerhof (PBE) functional (Perdew et al., 1996). The All Electron Relativistic (AER) core treat method was adopted for the relativistic effect (Koelling and Harmon, 1977). The dual numerical atomic orbital augmented by a polarization function (DNP) was employed as the basis set (Delley, 1990). A smearing of 0.005 Ha orbital occupation was applied to speed up electronic convergence. The GGA + vdW approach with Grimme method was selected to describe the vdW interaction (Tkatchenko and Scheffler, 2009). The convergence tolerances of energy, maximum force, and displacement were 1.0 × 10^{-5} Ha, 0.002 Ha/Å, and 0.005 Å, respectively.